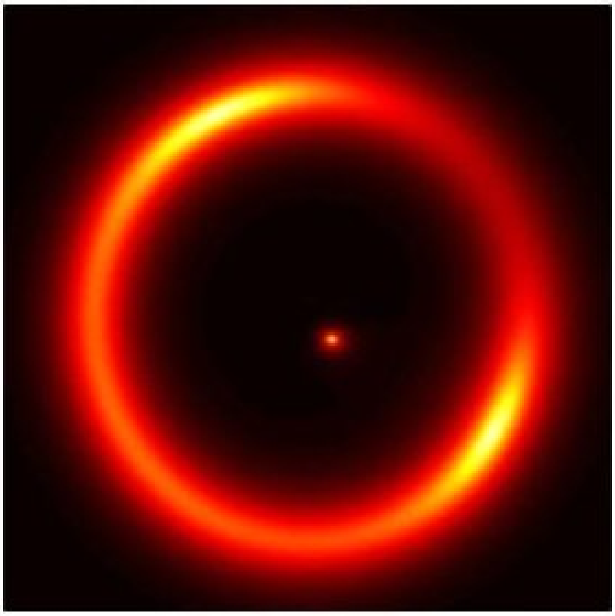

Refined modelling of the gravitationally lensed quasar PKS 1830-211

Master's thesis in Physics and Astronomy

Jaswanth Subramanyam

Department of Space, Earth and Environment
CHALMERS UNIVERSITY OF TECHNOLOGY
Gothenburg, Sweden 2019

MASTER'S THESIS 2019:NN

Refined modelling of the gravitationally lensed quasar PKS 1830-211

Jaswanth Subramanyam

CHALMERS
UNIVERSITY OF TECHNOLOGY

Department of Space, Earth and Environment
Division of Extragalactic Astronomy
CHALMERS UNIVERSITY OF TECHNOLOGY
Gothenburg, Sweden 2019

Refined modelling of the gravitationally lensed quasar PKS 1830-211

Jaswanth Subramanyam

© Jaswanth Subramanyam, 2019.

Supervisors:
Prof. Cathy Horellou, Department of Space, Earth and Environment
Dr. Sebastien Muller, Department of Space, Earth and Environment

Examiner: Prof. Cathy Horellou, Department of Space, Earth and Environment

Master's Thesis 2019:NN
Department of Space, Earth and Environment
Division of Extragalactic Astronomy
Chalmers University of Technology
SE-412 96 Gothenburg
Telephone +46 31 772 1000

Cover: Simulated image of the lensed quasar system PKS 1830-211 using GravLens.

Typeset in LaTeX
Printed by [Name of printing company]
Gothenburg, Sweden 2019

Refined modelling of the gravitationally lensed quasar PKS 1830-211
Jaswanth Subramanyam
Department of Earth, Space and Environment
Chalmers University of Technology

Abstract

PKS 1830-211 is a well studied radio-loud quasar with a flat spectrum undergoing strong gravitational lensing by a foreground galaxy. At cm-wavelengths the structure of PKS 1830-211 consists of two lensed images separated by 1 arcsecond and connected by an Einstein ring. High-resolution radio continuum observations have revealed structural changes in both the NE and the SW images. The absorption spectra arising from the foreground galaxy, at $z = 0.89$, show temporal variations. It is very likely that the variations in the lines of sight are related to changes in the structure of the background source.
In this thesis we use a core-jet model of the background source and examine how variations in the illumination affect the absorption spectra. For this purpose, the lens system was divided into three parts: the source, the lens, and an absorption screen in the lens galaxy. The position of the jet was varied while keeping the lens and the absorption screen parameters constant. Temporal variations of the order of $\sim 1\%$ in the absorption spectra over a time scale of ~ 1 yr corresponding to a physical scale of about ~ 0.3 pc, for a jet travelling at speed of light at the redshift of the source, could be reproduced with the model. This supports the claim that variations in the source structure can explain the observed temporal variations in the absorption spectra.

Keywords: Gravitational lensing, Einstein ring, PKS 1830-211, Absorption spectra, GravLens, modelling.

Acknowledgements

Firstly, I would like to thank Prof. Cathy Horellou for her advice and support from the beginning of my Master degree and through the thesis as my supervisor. For recognising my passion for astronomy and providing me with guidance throughout my degree as the Program Coordinator for the Physics and Astronomy Master. Also for offering me this topic for my thesis work.
Secondly, I would like to thank Dr. Sébastien Muller for the many hours of enthusiastic and illuminating discussions. For the kind support and input at every stage of the thesis work.
I would also like to thank Onsala space observatory for allowing me to visit the observatory when required and be a part of the wonderful scientific community at the observatory.
Finally, I would like to thank Chalmers University of Technology for giving me the opportunity to pursue my Master degree in astronomy. I would also like to thank my family for the infinite support and encouragement.

Jaswanth Subramanyam, Gothenburg, July 2019

Contents

List of figures

List of tables

1

Introduction

Gravitational lensing is an effect observed due to the bending of space-time due to the presence of mass. The problem of gravity bending light was stated as early as 1704 by Sir Isaac Newton in the first edition of Opticks : *"Do not Bodies act upon Light at distance, and by their action bend it's Rays; and is not this action (caeteris paribus) strongest at least distance?"*(Schneider et al. (1992)). The first discovery of a gravitational lens system was published in Walsh et al. (1979), titled "0957 + 561 A, B - Twin quasi-stellar objects or gravitational lens" (lens system Q0957+561 today).

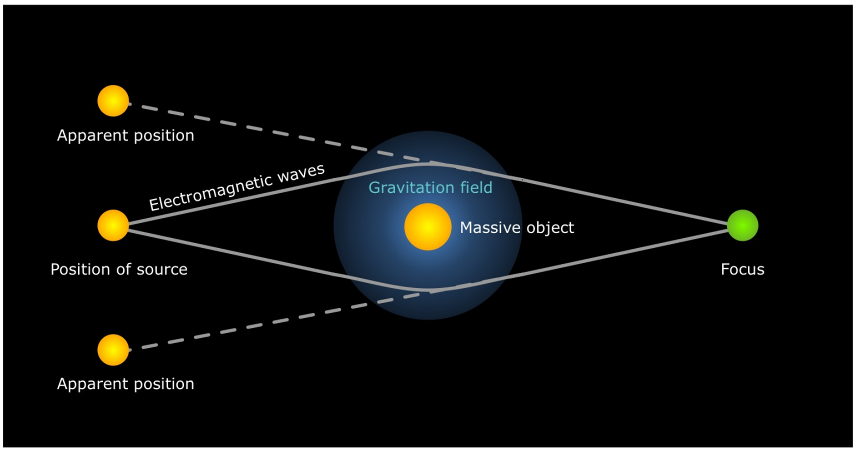

Figure 1.1: A typical scenario of gravitational lensing. (Image: German Aerospace Center - Deutsches Zentrum für Luft- und Raumfahrt; DLR)

A schematic representation of a lens system is shown in Figure 1.1. The figure shows light rays coming from a background galaxy deflected by a massive object in the line of sight of the observer. This leads to the observer seeing two different images of the background galaxy. The effect is understood by the relativistic formalism developed by Einstein (discussed in Chapter 2). Due to to the different path lengths covered by the light rays, the images from the source are observed with a certain time delay.

The focusing effect of lensing magnifies the images of the background galaxy. This allows us to observe distant and faint galaxies by acting as a cosmic telescope. In case of lens systems with a bright background source, we can even observe the absorption spectra from the interstellar medium (ISM) present in the foreground galaxy. One such case of a radio bright system, PKS 1830-211, was chosen for this thesis not only because of its flat continuum emission but also because of the large variations observed in the system on short time scales ($\leq$ 1 year).

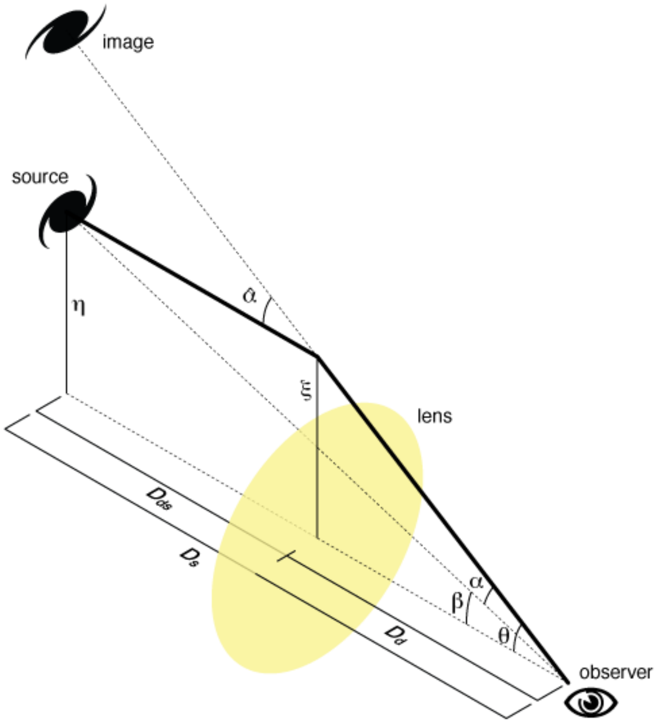

Figure 1.2: The angles involved in the case of a thin gravitational lens system. (Image: Sachs 2008)

The case of lensing due to galaxies at high redshifts is used in this thesis. For such cases the assumption of a thin gravitational lens comes into play. The distances between the source, lens and the observer are large enough that the thickness of the lens galaxy becomes negligible. Figure 1.2 shows the case of lensing with a thin gravitational lens.

The formalism required to understand the effect of gravitational lensing is presented in Chapter 2. Details about the lens system PKS 1830-211 are presented in Ch.3. Lens models used to simulate the lens system and the absorption spectra are presented in Chapter 4.

2

Gravitational lensing

Gravitational lensing enables a way of 'weighing' the cosmic objects (stars, galaxies, galaxy clusters etc.,) and the magnifying effect makes it a crude telescope to view the background source. Observationally, there is a lot of difficulty when it comes to gravitational lensing. The problems being:

- The strict alignment requirements to produce multiple lensed images is a rare phenomenon that occurs in less than one percent of the high-redshift sources. (Press and Gunn 1973)
- The large magnification ratios distort the original source morphology and lens models are required to analyze the source.
- The uncertainties in the lensing properties due to the ambiguity in the mass distribution of the lens.
- The possible presence of several massive objects or inhomogeneities in the line of sight will cause unknown distortions in the images and make the modelling difficult.

But despite these difficulties, numerous lensed systems are known today that have been used to study and test the theory behind lensing. This chapter deals with the formalism required to understand this phenomenon.

2.1 Lensing equation and magnification

The effect of gravitational lensing is well understood using Einstein's theory of General Relativity. The amount of deflection can be easily calculated if the positions of the source and the lens are well known, using Einstein's deflection law. The law states that for a light ray passing by an object of mass M, at a minimum distance ε; the angle of deflection α (Einstein's angle) is given by

$$\alpha = \frac{4GM}{c^2\varepsilon} = \frac{2R_s}{\varepsilon}. \tag{2.1}$$

The parameter R_s is called the Schwarzschild radius. Lensing occurs under the condition that $\varepsilon >> R_s$. This condition implies that $\alpha << 1$, enabling us to denote the total deflection produced by a mass distribution as the sum of the individual deflection angles. The equation 2.1 can be re-written for an ensemble of mass as

$$\alpha = \frac{4GM}{c^2} \int d^2\varepsilon \int dr'_3 \rho(\varepsilon'_1, \varepsilon'_2, r'_3) \frac{\varepsilon - \varepsilon'}{\mid \varepsilon - \varepsilon' \mid^2} \tag{2.2}$$

for a surface mass density given by

$$\Sigma(\varepsilon) = \int dr_3 \rho(\varepsilon_1, \varepsilon_2, r_3) \tag{2.3}$$

where r_3 indicates the component along the line of sight.

Combining this definition with equation 2.2, the angle of deflection can be written as

$$\alpha = \frac{4G}{c^2} \int d^2\varepsilon' \Sigma(\varepsilon') \frac{\varepsilon - \varepsilon'}{\mid \varepsilon - \varepsilon' \mid^2}. \tag{2.4}$$

Let us consider a geometry as shown in figure 2.1, where D_d is the distance from the observer to the lens, D_s is the distance from the observer to the light source, D_{ds} is the distance between the source and lens. For a light ray originated at the source with a position vector η and impact parameter ε, the angle of deflection is given by α. The angular distance between the lens and the source is given by β and the distance between the lens center and the lensed image is given by θ. The angle β also corresponds to the angular position that would have been observed in case of no lensing.

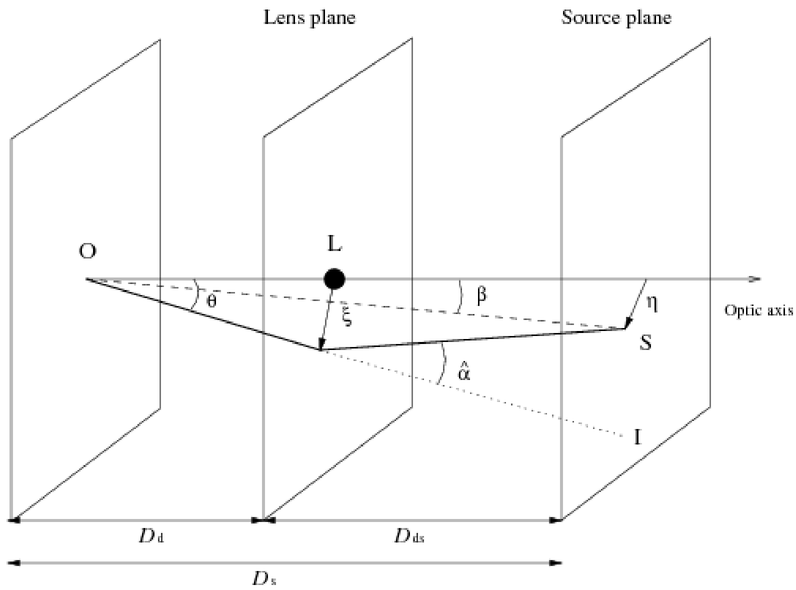

Figure 2.1: Angles involved in a typical gravitational lens system. (Image: Umetsu 2010)

As stated above the definition of the angle of deflection is valid for $\alpha << 1$, in which case using the small angle approximation, the angle of deflection can be read from figure 2.1 as

$$\eta = \frac{D_s}{D_d}\varepsilon - D_{ds}\alpha(\varepsilon) \tag{2.5}$$

Using angular coordinates, η and ε can be written as $\eta = D_{ds}\beta$ and $\varepsilon = D_d\theta$. With this equation 2.5 can be written as

$$\beta D_s = \frac{D_s}{D_d}\varepsilon - \frac{2R_s}{\varepsilon}D_{ds}. \tag{2.6}$$

Also using the angular coordinate definition of ε, equation 2.4 can be written as,

$$\alpha(\theta) = \frac{4G}{c^2}D_d \int d^2\theta' \Sigma(\theta') \frac{\theta - \theta'}{\mid \theta - \theta' \mid^2}. \tag{2.7}$$

Substituting this in equation 2.6, the lens equation can be rewritten in terms of the scaled deflection angle $\alpha(\theta)$ as

$$\beta = \theta - \alpha(\theta). \tag{2.8}$$

We can see that the equation 2.8 is analogous to mapping a point ε in the source plane to a point θ in the image plane.
The scaled deflection angle is formulated using the dimensionless surface mass density $\kappa(\theta)$ as

$$\alpha(\theta) = \frac{1}{\pi}\int d^2\theta' \kappa(\theta') \frac{\theta - \theta'}{\mid \theta - \theta' \mid^2} \tag{2.9}$$

where

$$\kappa(\theta) \equiv \frac{\Sigma(D_d\theta)}{\Sigma_{cr}} \tag{2.10}$$

and

$$\Sigma_{cr} \equiv \frac{c^2}{4\pi G}\frac{D_s}{D_d D_{ds}}. \tag{2.11}$$

The critical surface mass density Σ_{cr} depends only the distances involved in the lensing system.

2.1.1 Lensed images and magnification

Gravitational lensing is a geometry dependent phenomenon that is very sensitive to the relative positions of the source and lens for a static observer. Deflection of light due to gravitational lensing does not change the specific intensity I_ν as it is not connected to either emission or absorption. The specific intensity remains the same when seen by two observers with no relative frequency shift between each other. It only changes the flux density.

The light rays originated from the source undergo differential deflection by the lens and as a result the shape of the source is substantially changed in the lensed images.

$$A(\theta) = \frac{\delta\beta}{\delta\theta} = \left(\delta_{ij} - \frac{\delta^2\psi(\theta)}{\delta\theta_i\delta\theta_j}\right) = \begin{pmatrix} 1-\kappa-\gamma_1 & -\gamma_2 \\ -\gamma_2 & 1-\kappa+\gamma_1 \end{pmatrix} \tag{2.12}$$

where γ_1 and γ_2 are shear parameters defined by the deflection potential ψ and κ is the convergence or the dimensionless surface mass density. The convergence and the deflection potential are related by the two dimensional Poisson equation as shown below,

$$\Delta^2\psi = 2\kappa \tag{2.13}$$

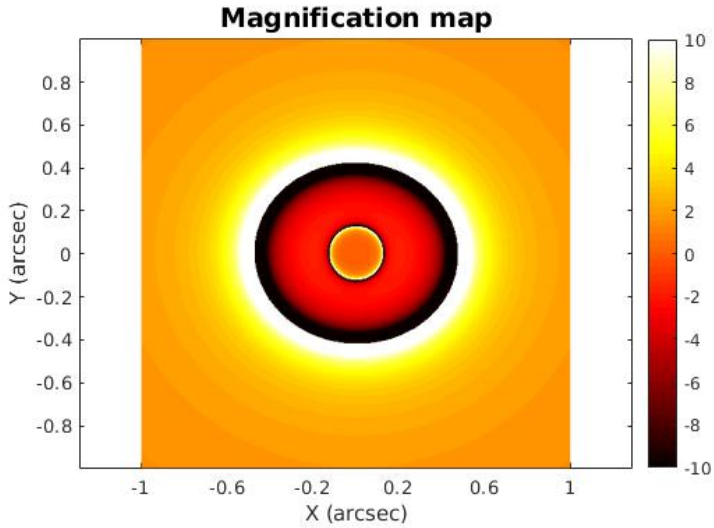

Figure 2.2: Magnification (μ) map for the lens model of PKS 1830-211 with the parameters shown in table 4.2 generated using GravLens. (The range of magnification ratios has been set to 10 to -10 to see the variations clearly)

The magnification μ is measured as the ratio between the flux from the image and the flux from the unlensed source. The magnification can be written in terms of the distortion matrix as

$$\mu = \frac{1}{detA} = \frac{1}{(1-\kappa)^2 - \mid \gamma_1 \mid^2} \tag{2.14}$$

The magnitude and the sign of μ varies at all points in the image and plays an important role. The lensed images have magnification values that are both positive and negative (two parities). The figure 2.2 shows the magnification in the lens plane for a simple lens model generated using GravLens. As it is clearly seen, the parity and the magnitude of magnification changes depending on the position. At certain points on the image plane the value of magnification diverges, these are known as *critical points*. A line joining the critical points in the image plane is called a *critical line*. These critical lines separate regions with different parities in the image plane.

The image of the critical lines in the source plane are called *caustics*. While the critical lines separate regions of different parities, the caustics separate regions that produce different number of images for a given lens model. The number of images after lensing changes by two when the source crosses over a caustic. Typically a well aligned lensed system can have three to five images.

An Einstein ring is a special case where the source and the lens are closely aligned and the lensed image is stretched out to a circle around the circumference of the lens. A small exercise by changing the position of the source from outside both the caustics to inside the two caustics clearly shows the changes in the number of images for each case.

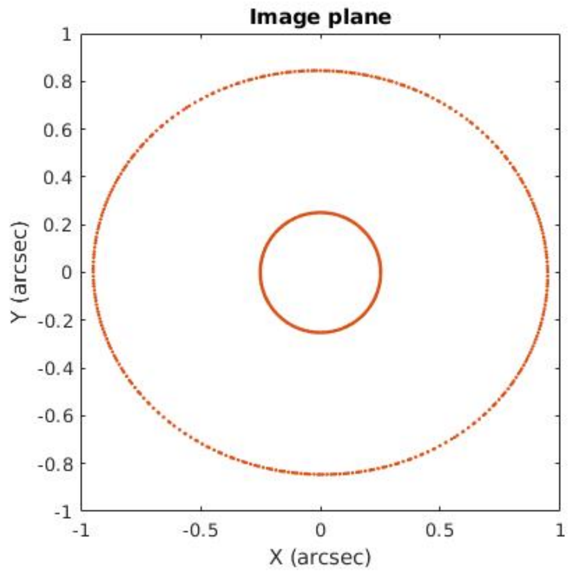

Figure 2.3: Critical lines for the lens model of PKS 1830-211 with the parameters shown in table 4.2 generated using GravLens.

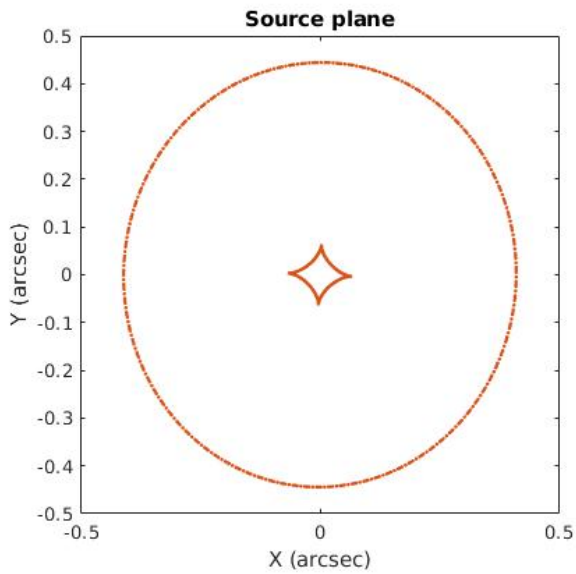

Figure 2.4: Caustics in the source plane that correspond to the critical lines shown in figure 2.3.

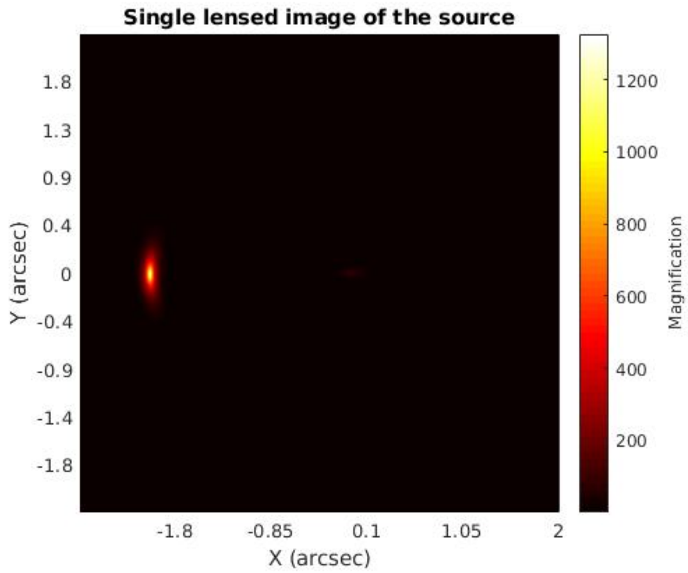

Figure 2.5: Single lensed image formed for a the source positioned outside both the caustics on the source plane.

For the first case, shown in figure 2.5, the source was positioned at $(x, y) = (-0.5'', 0'')$, which is a point on the x axis outside both the caustics in the source plane. We see a single lensed image of the source.

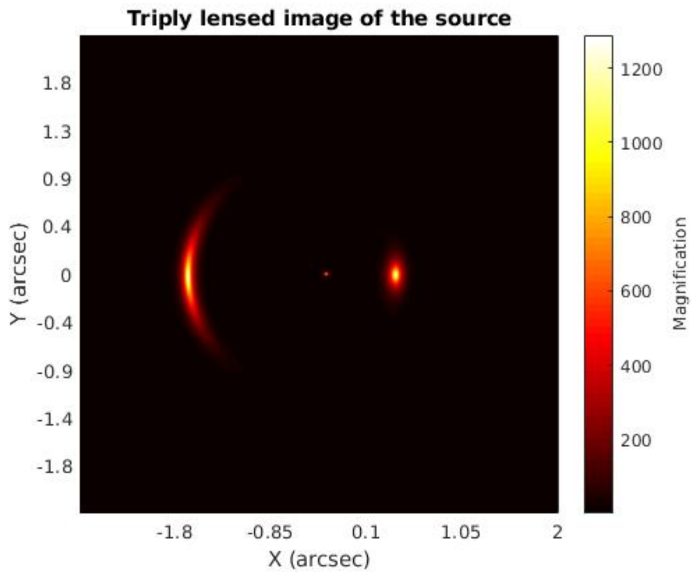

Figure 2.6: Triply lensed image formed for a source positioned outside one caustics and inside the other on the source plane.

For the second case, shown in figure 2.6, the source was positioned at $(x, y) = (-0.2'', 0'')$, which is a point on the x axis inside the first caustic and outside the second (inner) caustic in the source plane. We see that the number of images is indeed increased by a factor of two and we see a triply lensed image of the source.

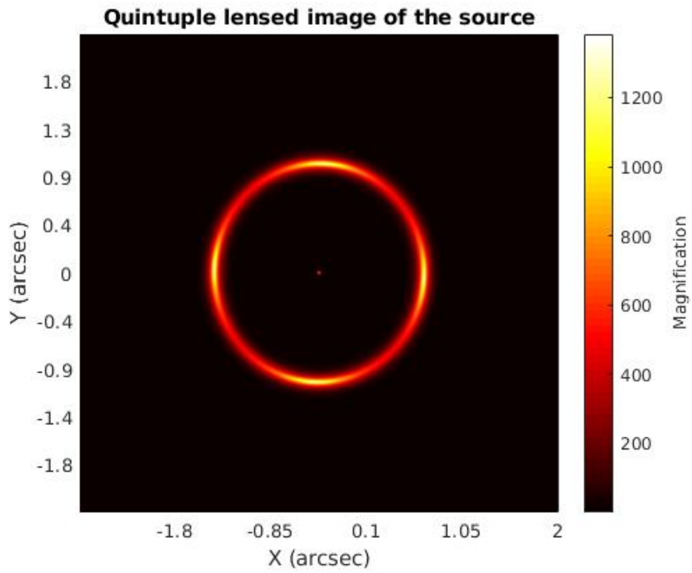

Figure 2.7: Quintuple lensed image formed for the position of the source inside both the caustics on the source plane. In this case the source was fully aligned with the lens so we also see a complete Einstein ring.

For the third case, shown in figure 2.7, the source was positioned at $(x, y) = (0'', 0'')$, which coincides with the position of the lens and is a point inside both the caustics in the source plane. We see that the number of images is again increased by a factor of two and we see a quintuple lensed image of the source with four images in the Einstein ring and one close to the center. As the source and the lens are fully aligned in this case, we see the emergence of an Einstein ring.

2.1.2 Time delay and Hubble constant

The light rays from the source experience different time delays as the light rays have different path lengths before reaching the observer. Estimates presented in Dyer and Roeder (1980) show that time delays vary from a range of 0.03 years to 1.7 years. Also concluding that the time delay is extremely sensitive to the exact position of the lens center.

The difference between the travel time of two distinct rays is proportional to the Hubble constant (H_0). The Hubble constant can be derived if all the concerned angles are well known through simple geometry. This exercise was not done as a part of the thesis.
The large scale effects can be easily be modelled by a quadratic lens model and the effect of fluctuations on small scales is also limited. However, the parameterized models of lensing is very sensitive to the mass distribution in the lens on the scales of image separation. To be able to generate a good estimate of H_0, we require an accurate time delay measurement, a well-identified lens whose redshift and velocity dispersion are also well known.

3

PKS 1830-211

This chapter deals with the details regarding the lens system PKS 1830-211 studied and modelled as a part of this thesis.

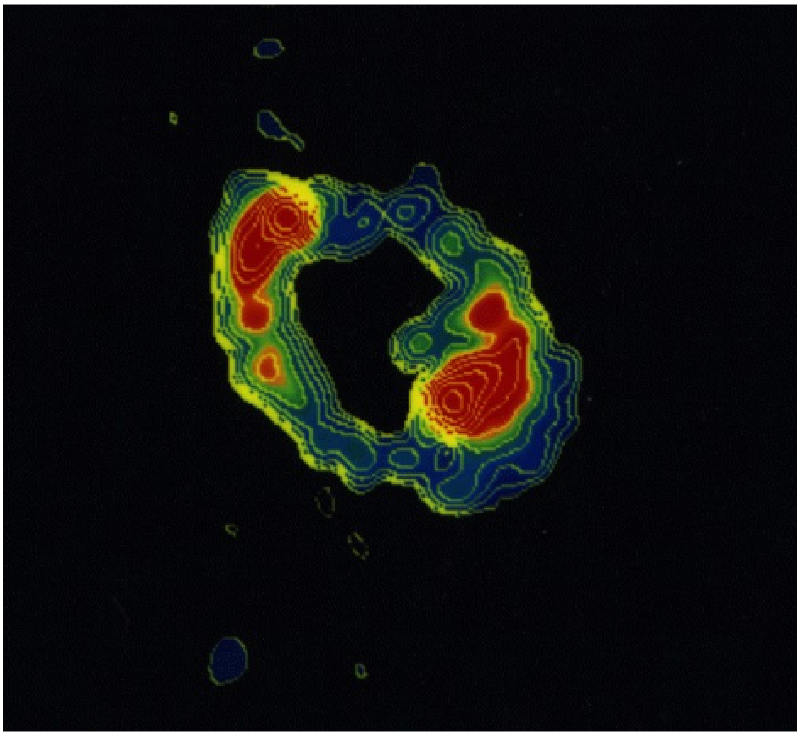

Figure 3.1: 5 GHz image of PKS 1830-211 at a resolution of 100 mas taken with Multi-Element Radio Linked Interferometer Network (MERLIN). (Image: Patnaik et al. 1993)

3.1 Introduction to PKS 1830-211

PKS 1830-211 was first identified as a gravitationally lensed object by Subrahmanyan et al. (1990) using VLA observations. They decomposed the north-east (NE) and south-west (SW) components into a core-jet-knot structure and built the first lens model. PKS 1830-211 is a well studied radio-loud quasar with a flat spectrum undergoing strong gravitational lensing by a foreground galaxy. The background source of PKS 1830-211 is a blazar, a quasar with a jet pointing nearly towards the Earth, at a redshift of $z = 2.57$. The foreground lens is at spiral galaxy at a redshift of

$z = 0.889$. PKS 1830-211 lies close to the Galactic plane ($b = -5.7°$), hence obscured in optical wavelengths due to Galactic dust extinction.

Due to this, the position of the lens center is highly uncertain and none of the currently existing models agree upon a single position for the lens. The currently existing models predict a nearly face-on spiral galaxy with an inclination angle of (17°-32°) for the H I disk of the lens galaxy (Koopmans and de Bruyn 2005). One other distinct feature of PKS 1830-211 is that it has a full Einstein ring encompassing the two lensed images separated by 1 arcsecond as shown in figure 3.1.

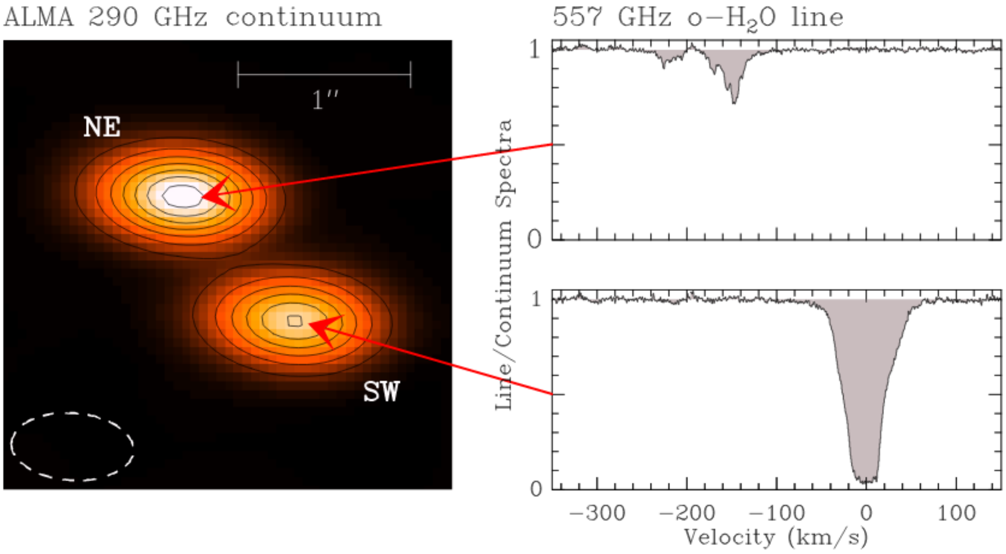

Figure 3.2: Left: 290 GHz continuum emission map of PKS 1830-211 from ALMA shown in Muller, Combes, et al. (2014), with well separated NE and SW images. The Einstein ring is not seen at mm wavelengths due to it's spectral index. Right: The absorption of fundamental ortho-water transition at 557 GHz of each lensed image separately.

The work presented in the master thesis of Sridhar (2013) concludes that the lensing effect due to the galaxies in the line of sight and the micro-lensing effect due to stars in our galaxy play a negligible role in the lensing scenario for PKS 1830-211. This raises the questions about the variations observed in the lensed images of PKS 1830-211.

3.2 Temporal variations observed in the spectra

Due to the effect of gravitational lensing there is an inherent time delay between the NE and SW images as the light from each image travels a different path length before it reaches the observer. This time delay can be well accounted for with a good lens model. In the case of PKS 1830-211 this is about for PKS 1830-211 is about

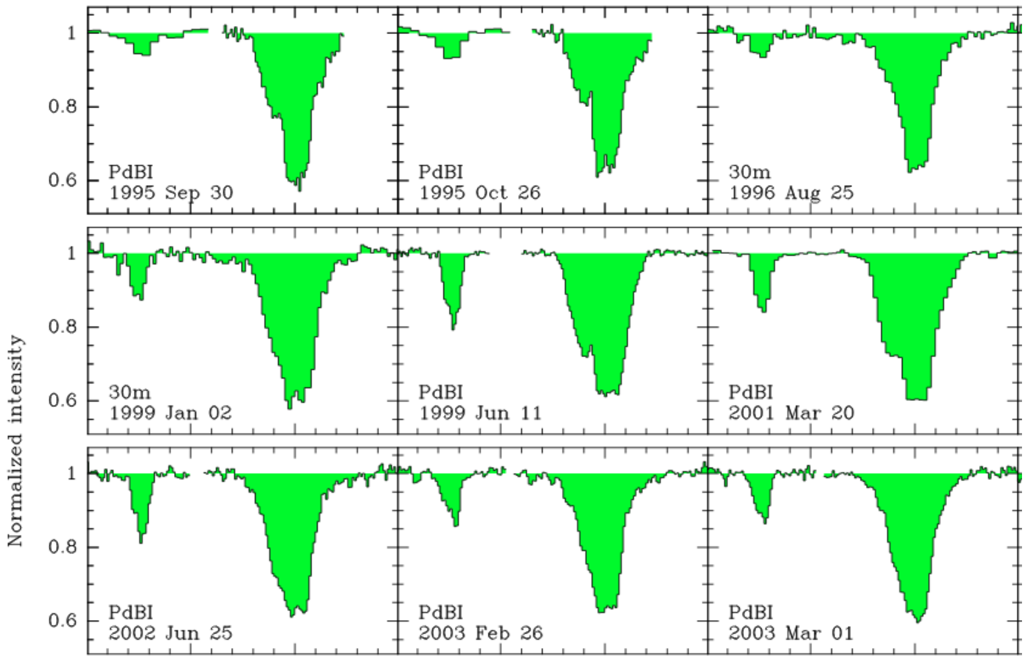

Figure 3.3: Variations in the HCO+(2–1) absorption spectra from PKS 1830-211 during a period from 1995 to 2003. An excerpt from the spectra presented in Muller and Guélin (2008). The spectra were obtained with either the Plateau de Bure Interferometer (PdBI) or the Institute for Radio Astronomy in the Millimeter Range (IRAM) 30 m telescope.

26^{+4}_{-5} days. However, absorption spectra from the lensed images of PKS 1830-211 show non-periodic variations in the flux ratio and the absorption spectra.

Muller and Guélin (2008) present the changes observed in the HCO+ and HCN (2-1) absorption lines of PKS 1830-211 after a 12-year-long survey. The NE image showed an increase in line depth by a factor ~ 3 over a period of one year from 1998-1999. The same line depth was observed to decrease by a factor of ≤ 6 from 2003 to 2006. The same variations were seen in the wings of the absorption lines of the SW image. Observations from VLBA used in Jin et al. (2003) show that the separation between the NE and SW images increased by 0.2 mas in a few months. Such changes in the absorption spectra can certainly not be associated with the inherent time delay from lensing.

Allison et al. (2017) studied H I and OH absorption lines from PKS 1830-211 and showed that the equivalent width of the H I component varies by a few percent on the scale of one year. They concluded that the manner of change is coherent between the NE and SW components, which implies that the variability is due to the change in the intrinsic brightness of the background source. In case of microlensing or interstellar scintillation, the variations in the two components would be independent of each other.

The possible sources of the variations in the absorption spectra could then be identified as the structural variations in the source. Changes in the illumination could occur in case of ejection of hot plasmons in the form of a jet. The exact reason is yet to be determined but we looked at the structural variations of the source as a possible solution and to try to understand the effects of such variations. A model was developed as a part of this master thesis to simulate the changes in the source for a given ISM screen in the foreground galaxy.

4
Methods

Here we present the method used to build the lens model for PKS 1830-211. For this purpose we used the publicly available code GravLens to emulate the effect of gravitational lensing. Following which we modeled the absorption spectra of the intervening galaxy. The full code developed for the model is available in the Appendix.

4.1 GravLens

GravLens is a code package developed by Chuck R. Keeton (Rutgers University) for the CfA-Arizona Space Telescope LEns Survey (CASTLES) of gravitational lenses.The algorithm for solving the lens equation and the techniques for constraining the lens model are given in Keeton (2011). The software and the manual for GravLens can be found in the homepage of GravLens.[1]

The functionality of the code can be divided into three simple sections, modelling the source, lens and producing the lensed images. All the calculations are unit-less and hence can be scaled to any physical units (pc, kpc, Mpc, etc.). The code requires a cosmological model to set up the environment for the simulations; the values of Hubble constant and cosmological constants can be given as an input to set up the environment. The code package has default values set for these parameters that will be used if nothing is mentioned by the user.

GravLens uses recursive gridding to divide the sample space into minor grids. First a coarse grid is plotted throughout the environment followed by a finer grid within the first at points with non-zero flux intensity i.e, near the source and images. GravLens simulates lensing by tracing the path of a light rays originating at the source and travelling to the plane of the observer.

Besides fully simulating a gravitational lens, GravLens also provides the opportunity to retrace the position and the flux density of the source for a given lensed image as an input. GravLens documentation provides commands for all the steps required for the simulation.

The lens model for PKS 1830-211 presented by Winn et al. (2002) was adopted for the simulations in this thesis work based on the thesis work of Sridhar (2013). The

[1] http://redfive.rutgers.edu/ keeton/gravlens/

parameters used for modelling PKS 1830-211 are mentioned in the table 4.1

Parameter	Value
Ellipticity	0.091±0.009
Lens orientation	86.1°± 3.1°
Unlensed source position	(0".264,-0".418)±0".005
Lens center (x,y)	(+0".328,-0".486)
Hubble constant	$44 \pm 9\ km/sMpc^{-1}$

Table 4.1: Parameters of the lens model taken from Winn et al. (2002).

4.1.1 Simulating the source

The source can be simulated using various light distribution models available in GravLens. The position in x and y, the scale radius and the power law for the intensity variation are required as inputs by the user to generate a model for the source. The code package simulates a source at the given position in the 3 dimensional distance from the observer based on the redshift value for the source that is also given as an input. The user can set any number of sources at different redshifts in the environment and generate the effect of their lensing. The code generates a map of the caustics in the source place using recursive gridding, as shown in figure 2.4.
For a given source flux, the luminosity distributions can be simulated using three types of models. Point source, constant surface brightness and a Sérsic intensity distribution model given by the following equation:

$$I(R) = I_e exp\Big(- b_n \Big[\Big(\frac{R}{R_e}\Big)^{1/n} - 1 \Big]\Big) \tag{4.1}$$

A Sérsic profile describes the variation of the intensity of a galaxy with the radius derived from a generalization of de Vaucouleurs' law. Figure 4.1 shows the various profiles of surface brightness for the index n. Most galaxies fit with a Sérsic profile index in the range $1/2 < n < 10$. Brighter galaxies tend to fit with larger values of n, however due to the fact that not much is known about the lens galaxy of PKS 1830-211, a general value of $n = 4$ was set. The value was based on the best fit estimate presented in Caon et al. (1993) on the shape of the light profiles of early-type galaxies.

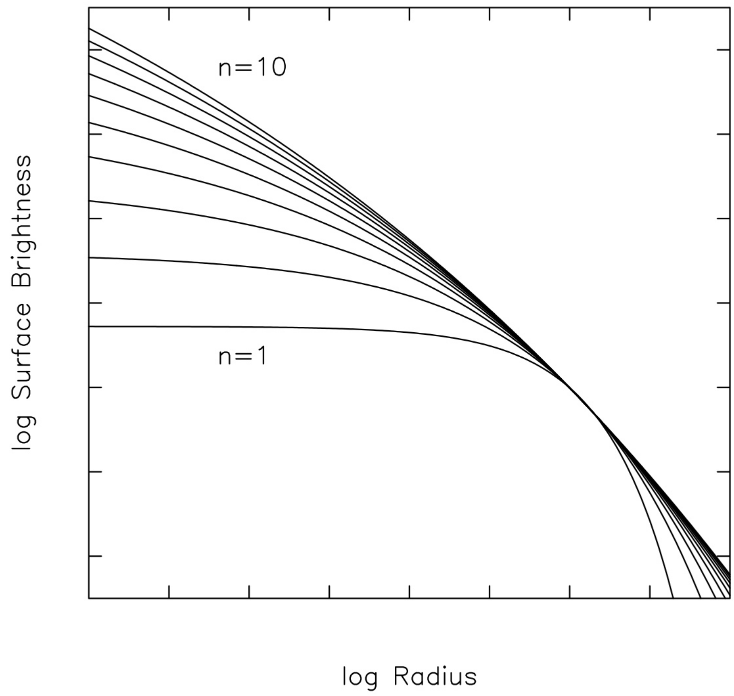

Figure 4.1: Variation of surface brightness with radius as a function of index n.

4.1.2 Simulating the lens

The lens system is simulated using a mass distribution, various mass models are available in GravLens to simulate different mass distributions shown in table 4.3. The code takes the position in x and y along with the mass, scale radius, redshift, mass model and related mass model parameters shown in figure 4.2. It generates a lens at the given position and redshift. The code also generates the magnification map and the critical curve map for the lens, as shown in figure 2.3.The model used for the simulation work in this thesis are presented in the next section.

p[1]	M	Mass scale
(p[2],p[3])	(x_0,y_0)	Position of galaxy
(p[4],p[5])	(e,θ_0)	Ellipticity parameters
(p[6],p[7])	(γ,θ_γ)	External shear parameters
(p[8],p[9])	(s,s)	Misc., often scale radii
p[10]	α	Misc., often power law index

Table 4.2: Input parameters for generating a lens model using GravLens.

The parameters for the canonical lens models vary depending on which mass model is chosen to simulate the lens.
Once the source and the lens have been set, Gravlens tracks the trajectory of a light ray originated at the source and all the way to the observer to $z = 0$. The codes takes an input of a finite number of light rays per grid that are to be used to generate

Parameter	Model
ptmass	Point Mass
alpha	Softened power law
devauc	De Vaucouleurs $r^{\frac{1}{4}}$ numerical model
nfw	Navarro Frenk White model
unidisk	Uniform density disk

Table 4.3: Various mass models available in GravLens

the lensed image. The code generates an output file in terms of luminosity flux at the observer position.

4.2 Lens model

The thesis work presented here follows up after the master thesis work by Sridhar (2013), where an extended study was made on the lensed images using different pre-existing models and understanding the effects of micro-lensing. The initial parameters for the lens model were primarily based on the model by Winn et al. (2002). Different pre-existing models were tested and the parameters of the models varied to understand the underlying degeneracy between the different input parameters. The goal of this thesis is to develop a model to simulate the variations in the absorption spectra.

Simulating the source and the lens is done using GravLens. For modelling the source, a Sérsic profile model was used to simulate the core-jet structure by placing two Sérsic sources. First one to simulate the source luminosity and the other to simulate the bright jet. GravLens allows the user to stack as many sources as needed as the effect of lensing from multiple sources on the same lens can be linearly summed.

For simulating the lensing galaxy, a Simple Isothermal Ellipsoid (SIE) model was used with the model parameters following Winn et al. (2002). The output from GravLens is obtained in the form of a lensed image using the inbuilt commands. The structural changes in the quasar can simulated using this section of the model. The lensed image is then taken as the input for the next section of the code where the absorption screen is simulated.

4.3 Modelling absorption spectra

The lensed image obtained from GravLens is taken as the background illumination for an absorption screen. The kinematic model of neutral hydrogen for the spiral lens galaxy of PKS 1830-211 presented in Koopmans and de Bruyn (2005) is taken as the reference for simulating the lens galaxy. The position, inclination and the rotation curve of the kinematic model was used.

The assumption of an optically thin axisymmetric H I disk was used in the modelling. In the first run the opacity was chosen to vary as a power law given by the equation 4.2 from Koopmans and de Bruyn (2005) model.

$$\tau(r) = \tau_0 \left(\frac{r}{r_0}\right)^{\gamma} \tag{4.2}$$

The kinematic center coincides with the position of the lens center, the inclination of the disc is also taken into account by multiplying the optical depth τ with a factor of $(\cos i^{-1})$. Also, the assumption of isotropic broadening of the H I absorption lines by an amount $\sigma_{H\,I}$(=FWHM/2.35). The observed broadened line profile is obtained from the convolution of the unbroadened profile with the Gaussian velocity profile as shown in the equation below

$$I(v) = I_0 \exp\Big(-\tau \exp\Big(\frac{-(v - v_{los})}{2\sigma_{H\,I}^2}\Big)\Big) \tag{4.3}$$

The following parameters were used in generating the kinematic model of the lens galaxy

Inclination angle (i)	20°
Position Angle (θ)	+11°
Velocity dispersion ($\sigma_{H\,I}$)	47 km/s
Opacity (τ_0)	0.057
Power law (γ) and r_0	3.62, 0.5”
Lens center(x,y) in arcsec	(+0”.328,-0”.486)

Table 4.4: Values chosen from the best fitting parameters of the kinematic models presented in Koopmans and de Bruyn (2005) for the lens model by Winn et al. (2002)

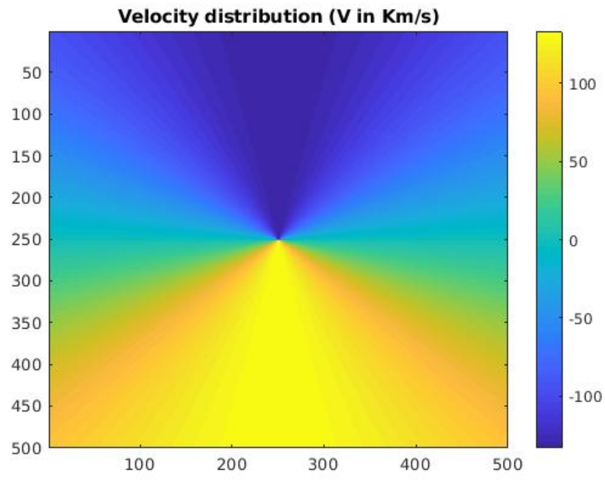

Figure 4.2: Velocity profile for the lens galaxy at an inclination of 20°

The velocity profile at an inclination of $20°$ as shown in the figure 4.2 was added to the opacity screen to simulate the effect of profile broadening due to galaxy rotation and using the equation **??** was used to generate the absorption profile. The simulated spectra are presented in the Chapter 5.

5

Results

5.1 Simulating PKS 1830-211

First, the model from Winn et al. (2002) was recreated using GravLens with the help of the commands from the GravLens manual. The environment for the simulations was setup by providing the values of Hubble constant, redhshift of the source and the lens galaxies and the cosmological constants as shown below:

```
set omega  = 0.3
set lambda = 0.7
set hval   = 0.7
set zlens  = 0.889
set zsrc   = 2.507
```

After the environment is setup, the size of the grids and the number of levels of sub gridding is also set. We set 2 levels of sub-gridding and go for a primary grid of 100 and a secondary grid of 1000.

```
set ngrid1 = 100
set ngrid2 = 1000
set maxlev = 2
```

Next, the parameters for the lens model are set from Winn et al. (2002) using the following set of commands:

```
startup 1 1
    alpha 1 0.0 0.0 0.091 87.1 0 0 0.1 0 1.0
    0 0 0 0 0 0 0 0 0 0
```

The *startup* command allows us to set up the number of galaxies per mass model and the number of mass models required for the model. For simulating PKS 1830-211, we chose 1 galaxy and one mass model to simulate the lens. The parameters of each galaxy are set in an individual command line following the startup command. The ten parameters required for each galaxy, shown in table 4.2, are given as input after the mass model for the galaxy. A softened power law potential was used for the mass model with the power law α set to 1 for PKS 1830-211. The *startup* command also sets up the initial tiling of the lens and the source plane.
setsource command is used to set the required parameters for the source.

```
setsource 2 100
    sersic 8 -0.064 0.046 0 0 0.05 0 1/4
    sersic 2 -0.0640002 0.046 0 0 0.01 0 1/4
    0 0 0 0 0 0 0 0
    0 0 0 0 0 0 0 0
```

The relative position of the source to the lens was set based on the parameters from table 4.1. GravLens allows us to set the number of sources and the number of light rays per grid that are to be used for the ray tracing. The number of sources was set to two to emulate a core and a jet model of the quasar of PKS 1830-211.

The lensed image from the model is obtained using the *SBmap2* command which generates a plot of the illumination flux for a specified field of view. The field of view (fov) and the number of pixels are provided with the *SBmap2* command, a fov of 1 square arcsec and 4000 pixels per dimension (x,y) were chosen to reach a physical scale of $\sim 1.5 - 2pc$ per pixel. The file type and the name are mentioned to specify the output format of the lensed image.

```
SBmap2 -1 1 4000 -1 1 4000 1 pks_winn.fits 3
```

Figure 5.1 shows the lensed imaged obtained using the procedure mentioned above.

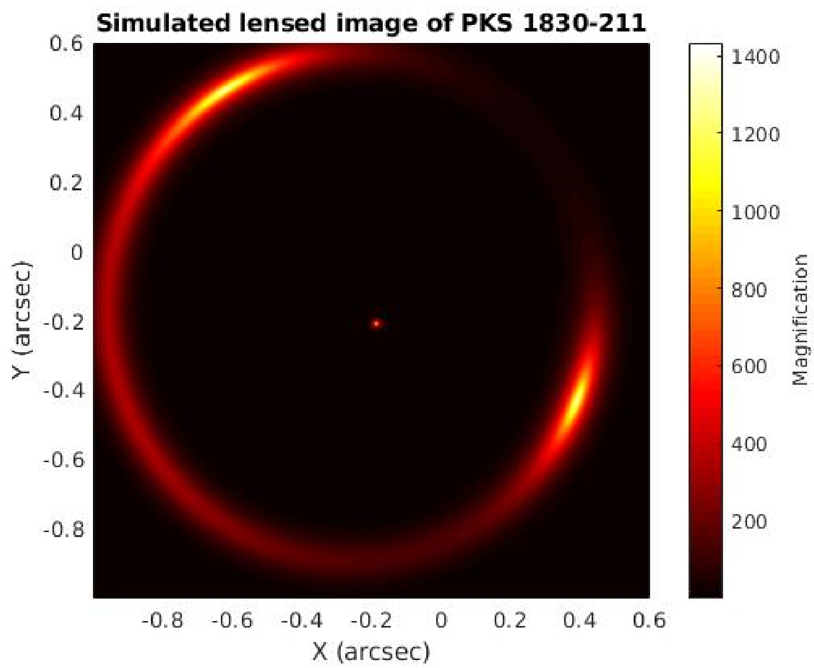

Figure 5.1: The lensed image of the quasar modelled using GravLens for the parameters given in Winn et al. (2002).

5.2 Simulating the absorption screen

The ISM screen developed using the method presented in section 4.3 was used to simulate the absorption spectra.The idea behind simulating the variations is that, the light from the ejected plasmons in the form of a jet will pass through different cross-sections of the galactic disc of the lens galaxy as the ejected plasmons are moving away from the core. Two different models of the absorption spectra were used to simulate atomic and molecular gas. For the atomic H I gas, a radially varying model was chosen using the formula shown in equation 4.2. The absorption spectra are integrated over the entire illuminating surface, the NE and SW images are resolved through kinematics alone.

Figure 5.2a shows the absorption spectra from PKS 1830-211 from WSRT for H I in the lens galaxy. This was recreated using the kinematic model parameters derived from these observations in Koopmans and de Bruyn (2005). The recreated absorption profile for H I is shown in figure 5.2b.

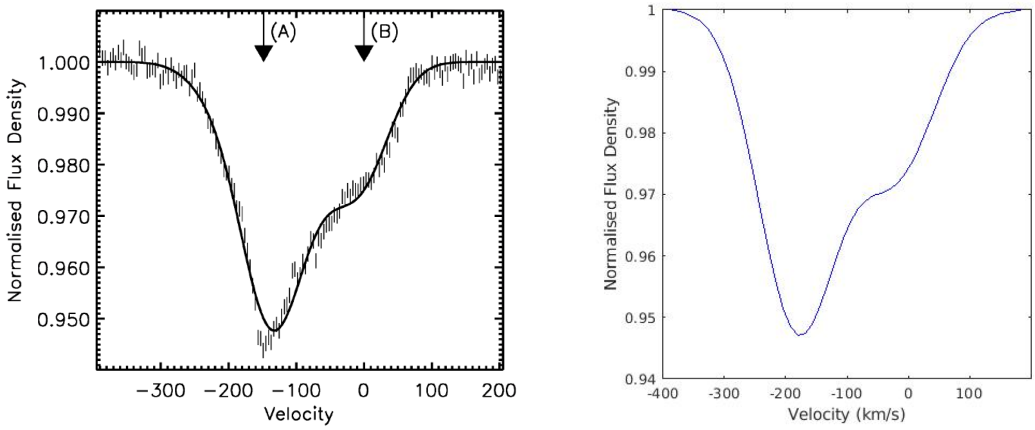

(a) H I spectra obtained from 753 MHz data from Westerbork Synthesis Radio Telescope (WSRT) presented in Koopmans and de Bruyn (2005).

(b) Absorption spectra simulated using the parameters from the Koopmans and de Bruyn (2005) model.

Figure 5.2: The H I spectra obtained from the simulations agree well with the spectra presented in Koopmans and de Bruyn (2005). The two peaks are centered around $v = -150$ km/s and $v = 0$ km/s.

For the case of H I gas, the jet in the source was moved by 1 milli arcsec away from the core to observe the changes in the spectra. The physical distance travelled by this jet at relativistic speeds for 1 mas at the redshift of the source ($z = 2.57$) is about ~ 8 pc and a time scale of 20 years.

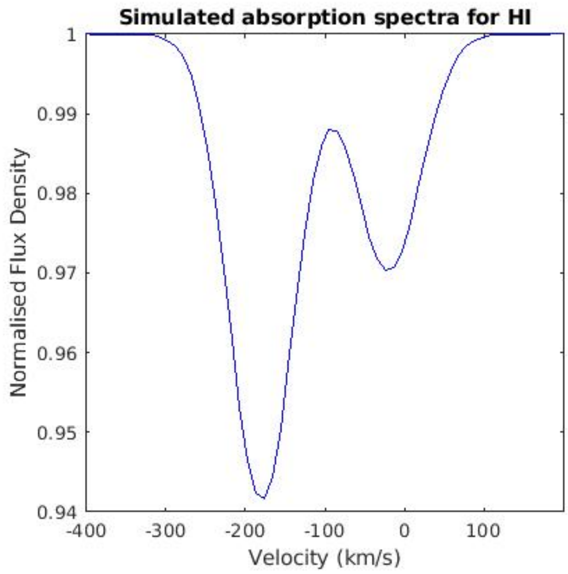

Figure 5.3: Absorption from both NE and SW images of PKS 1830-211, the peak on the left corresponds to the NE image and the right peak corresponds to the SW image. Plotted for the case of ISM screen made up of H I gas.

The spectra from the two positions of the jet were plotted over each other and shown in figure 5.4. The difference in the spectra was taken and as seen in figure 5.5, the spectra from each image is seen to have changed by different amounts. However, the amount of change observed in the images is too small to explain the changes seen in PKS 1830-211.

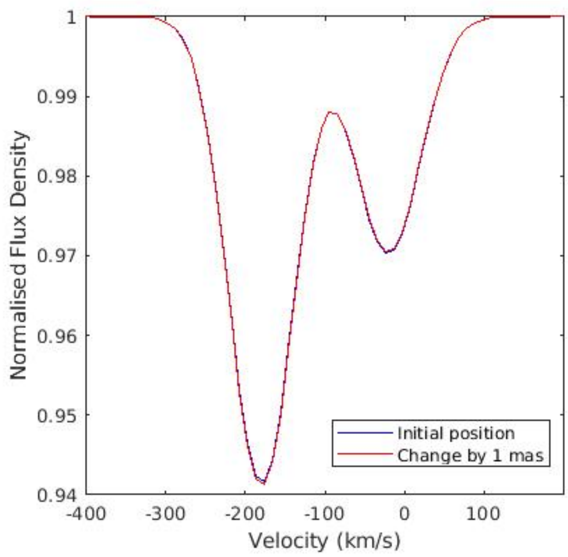

Figure 5.4: Comparison of the spectra of PKS 1830-211. Initial position referring to the case where the jet is starting at the core and the final position of the jet 1 mas away.

The time scale of variations and the distance moved by the jet in this case is too large to be realistic for the case of a relativistic jet. Allison et al. (2017) show the variations in the H I spectra on yearly scales and the variations seen in this simulation are much smaller in comparison. This could also imply that the jet is undergoing superluminal motion resulting in much smaller time scales.

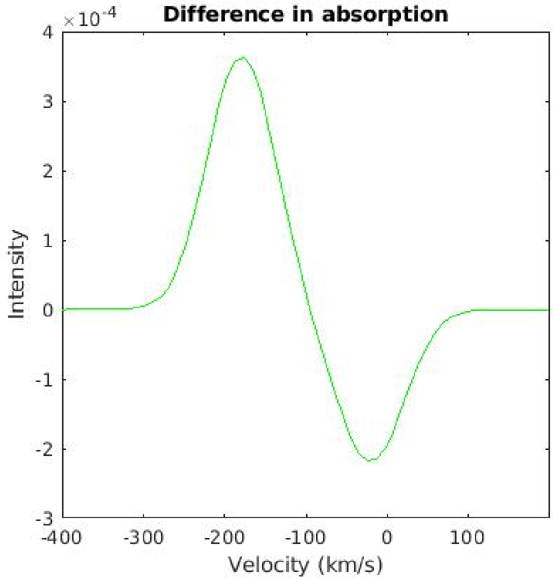

Figure 5.5: The difference between the absorption spectra for the two positions of the jet for an ISM screen with atomic gas.

For the molecular gas, a clump model was used to see the variations. Clumps of the size ~ 8 pc were placed in a checker grid configuration to emulate a distribution of clumpy molecular gas in the lens galaxy. Each pixel at this resolution corresponds to about ~ 2 pc, 4 pixels were grouped together to emulate a cloud of size about ~ 8 pc. The ISM grid used for this purpose is shown in figure 5.6a.

For the purpose of modelling the changes with an ISM screen consisting of molecular gas, much smaller and realistic scales of motions were taken. The position of the jet was changed to a maximum of 2 micro arcsec, which corresponds to a distance of $0.3pc$ at the source redshift and a time scale of 1 year for a jet travelling at the speed of light, superluminal motions up to $10c$ can be considered. The comparison of the spectra and the difference are plotted for this model of ISM screen and are shown in figures 5.8 and 5.9.

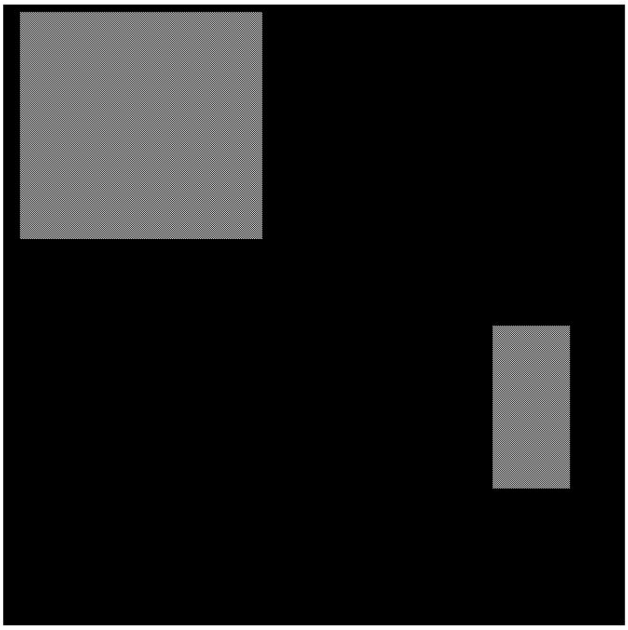

(a) Opacity screen used for simulating the absorption for the case of molecular gas.

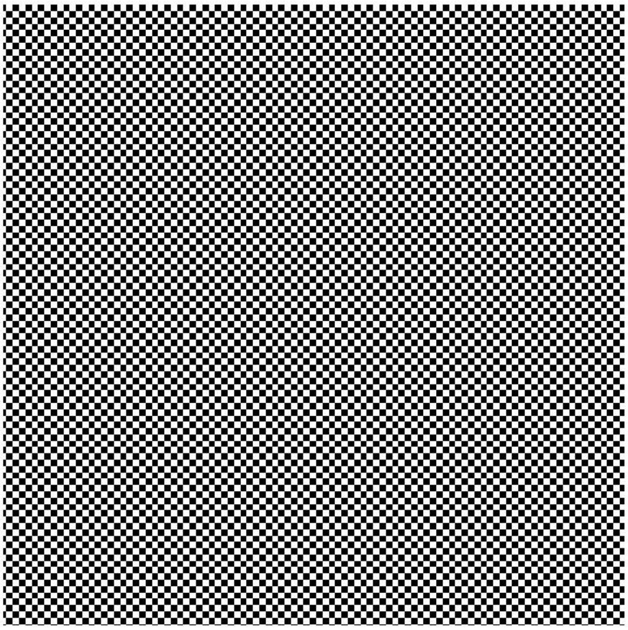

(b) Checker grid structure used for distributing the clouds within each grid.

Figure 5.6: Two smaller grids of size 1500x1500 pixels and 1000x500 pixels shown in (a) was used for the clumpy molecular ISM placed over the NE and SW images of PKS 1830-211 respectively.

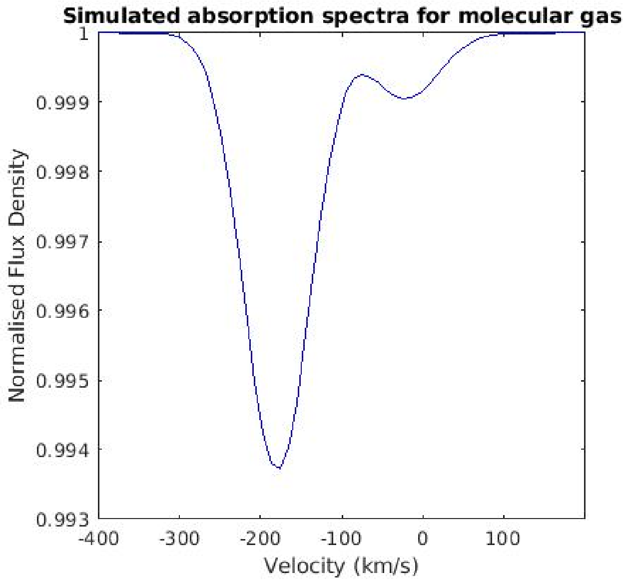

Figure 5.7: Absorption from both NE and SW images of PKS 1830-211, the peak on the left corresponds to the NE image and the right peak corresponds to the SW image.The absorption from each image is distinctly different due to the fact that they undergo differential magnification and the NE images is much brighter compared to the SW image. Plotted for the case of an ISM screen made of clumpy molecular gas.

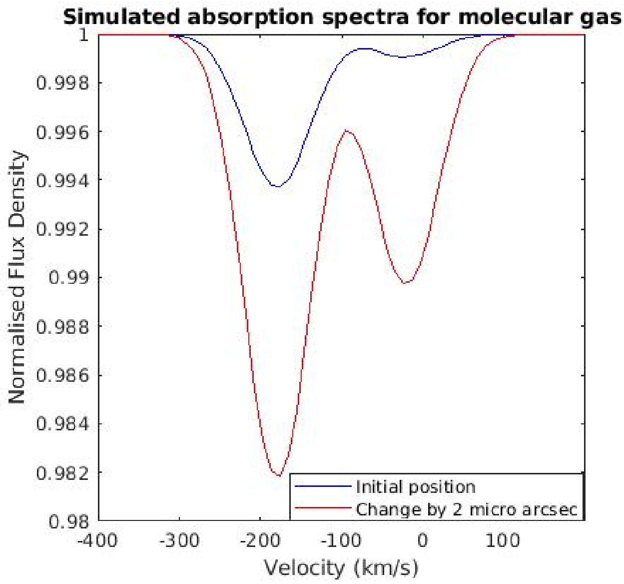

Figure 5.8: Comparison of the spectra of PKS 1830-211 integrated over the entire illuminating surface within the grid. Initial position referring to the case where the jet is starting at the core and the final position of the jet 2 micro arcsec away.

The absorption spectra is seen to vary by about $\sim 1\%$ for the case of a molecular gas, which is orders of magnitude larger than the difference seen in the case of atomic gas. This would lead us to the conclusion that the changes could be due to the varying illumination on a clumpy ISM screen made up of molecular gas.

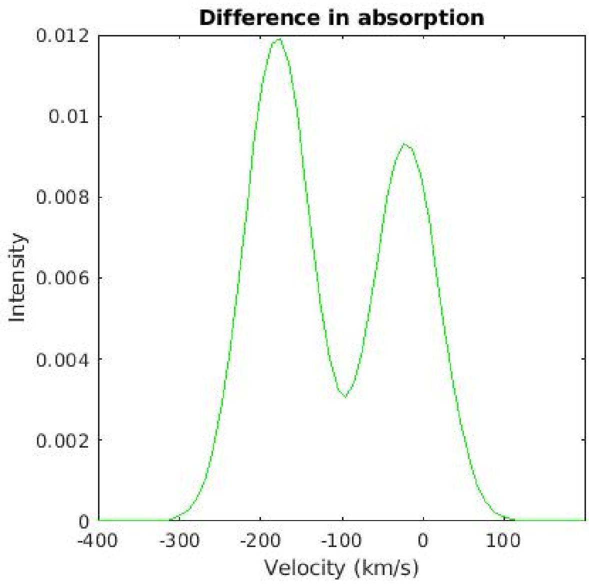

Figure 5.9: The difference between the absorption spectra for the two positions of the jet for an ISM screen with molecular gas.

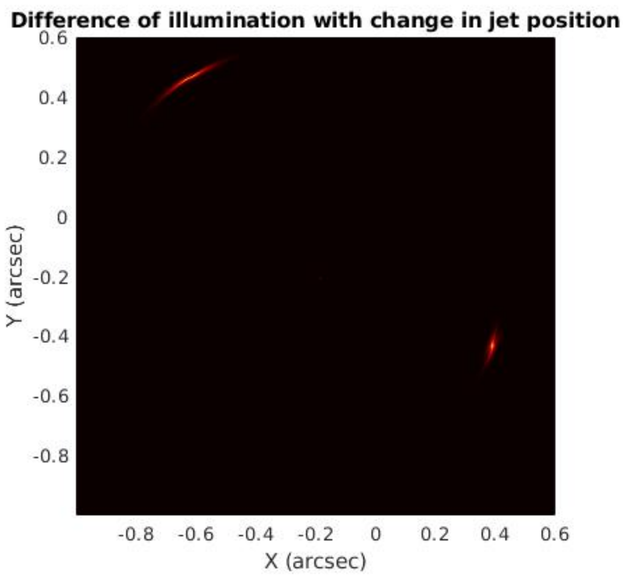

Figure 5.10: The difference in the background illumination for a jet motion of 2 micro arcsec.

By plotting the difference of luminosity between the lensed images, before and after moving the jet away from the core, we see that a total of 3092 pixels see an increment in luminosity in the vicinity of the NE image. 3019 pixels see a decrease in the luminosity in the same vicinity around the NE image. Similarly, for the SW image we see an increase in luminosity in 1888 pixels and a decrease in luminosity in 2069 pixels around the SW image.

5.3 Third image of PKS 1830-211

The theory of lensing predicts a third image close to the position of the lens center and it is clearly seen in the simulations done with GravLens. However, the nature of the third image is that it would be highly de-magnified compared to the NE and SW images, making it very difficult to observe directly with low sensitivity. Currently the existing observations of PKS 1830-211 do not detect the third image completely. Resolving this third image would help us to precisely pin point the location of the lens galaxy and help eliminate the uncertainty in the position of the lens center.

The de-magnification ratio of the third image will also provide a constraint for the mass distribution in the inner region ($\leq 1kpc$) of the lens galaxy Keeton (2003). Despite being highly de-magnified, it would be possible to observe the third image due to the intrinsic brightness of the source of PKS 1830-211 with a telescope like ALMA with high sensitivity and dynamic range. However, the detection of a continuum source close to the expected position of the third image could be ambiguous with the detection of dust emission from the lens galaxy. If third image is fully detected, it would be possible to definitely categorize the third image, either as the dust emission or the predicted third image.

A proposal to ALMA cycle 7 was submitted for high resolution sub-mm observations of PKS 1830-211 but unfortunately the proposal was not accepted this time. As of now, we do not much about the lens galaxy, i.e,. the star formation activity and overall molecular gas content. Hopefully, we will be able to get observation time with ALMA and shed light on these aspects of the lens galaxy.

6

Conclusion and future work

In the thesis we have modelled the gravitational lensed system PKS 1830-211, to investigate the time variations of the absorption spectra. For this purpose, the lens system was first modelled using GravLens with predefined parameters from existing models for the background quasar source and the intervening lens galaxy. A kinetic model of the ISM for the lens galaxy was built to simulate the absorption spectrum from the lens galaxy. Homogeneous and uniformly distributed gas models were first used following which a clumpy model with homogeneous clouds of $\sim 2pc$ was used.

From the simulations done in this thesis to vary the source illumination and the ISM absorption screen, we can come to the conclusion that the rapid variations observed in PKS 1830-211 could definitely be solely because of the structural variations in the quasar. Following the analysis done in Sridhar (2013), we can rule out the effect of microlensing and conclude by agreeing with Muller and Guélin (2008) that the variations observed in the spectra could be explained because of the changes in the quasar illumination.

An absorption screen was modeled in the intervening galaxy, either in the form of a smooth radially varying screen, well reproducing the distribution of atomic gas, and in the form of a clumpy screen, reproducing the distribution of molecular gas. If the ISM cloud was was uniformly distributed and homogeneous, we would not be able to see such large variations on time scales less than a year for a jet travelling at the speed of light. Hence, it can be concluded that the ISM screen in the lens galaxy consists of clumpy gas clouds of the scales of $\leq 10pc$.

As a part of the future work, obtaining high-resolution data of PKS 1830-211 to pin-point the position of the lens would definitely help refining the model of PKS 1830-211. Very high-angular mm VLBI observations of the quasar coupled with monitoring of the molecular absorption profiles from the lens galaxy, we can precisely track the change of illumination of the quasar and its effects on the absorption spectra.

Bibliography

Allison, J. R. et al. (2017). “Illuminating the past 8 billion years of cold gas towards two gravitationally lensed quasars”. In: *Monthly Notices of the Royal Astronomical Society* 465.4, pp. 4450–4467. DOI: 10.1093/mnras/stw2860. arXiv: 1611.00863 [astro-ph.GA].

Caon, N., M. Capaccioli, and M. D’Onofrio (1993). “On the shape of the light profiles of early-type galaxies.” In: *Monthly Notices of the Royal Astronomical Society* 265, pp. 1013–1021. DOI: 10.1093/mnras/265.4.1013. arXiv: astro-ph/9309013 [astro-ph].

Dyer, C. C. and R. C. Roeder (1980). “A range of time delays for the double quasar 0957 + 561 A, B”. In: *The Astrophysical Journall* 241, pp. L133–L136. DOI: 10.1086/183376.

Jin, C., M. A. Garrett, S. Nair, R. W. Porcas, A. R. Patnaik, and R. Nan (2003). “Changes in the measured image separation of the gravitational lens system PKS 1830-211”. In: *Monthly Notices of the Royal Astronomical Society* 340.4, pp. 1309–1316. DOI: 10.1046/j.1365-8711.2003.06390.x. arXiv: astro-ph/0301197 [astro-ph].

Keeton, Charles R. (2003). “Lensing and the Centers of Distant Early-Type Galaxies”. In: *The Astrophysical Journal* 582.1, pp. 17–29. DOI: 10.1086/344539. arXiv: astro-ph/0206243 [astro-ph].

– (2011). *GRAVLENS: Computational Methods for Gravitational Lensing.* ascl: 1102.003.

Koopmans, L. V. E. and A. G. de Bruyn (2005). “HI kinematics in a massive spiral galaxy at z= 0.89”. In: *Monthly Notices of the Royal Astronomical Society* 360.1, pp. L6–L9. DOI: 10.1111/j.1745-3933.2005.00030.x.

Muller, S., F. Combes, et al. (2014). “An ALMA Early Science survey of molecular absorption lines toward PKS 1830-211. Analysis of the absorption profiles”. In: *Astronomy Astrophysics* 566, A112, A112. DOI: 10.1051/0004-6361/201423646. arXiv: 1404.7667 [astro-ph.GA].

Muller, S. and M. Guélin (2008). “Drastic changes in the molecular absorption at redshift z = 0.89 toward the quasar PKS 1830-211”. In: *Astronomy Astrophysics* 491.3, pp. 739–746. DOI: 10.1051/0004-6361:200810392. arXiv: 0810.0378 [astro-ph].

Patnaik, A. R., T. W. B. Muxlow, and D. L. Jauncey (1993). “MERLIN 5-GHz observations of PKS1830-211”. In: *Liege International Astrophysical Colloquia.* Ed. by J. Surdej, D. Fraipont-Caro, E. Gosset, S. Refsdal, and M. Remy. Vol. 31, p. 363.

Press, William H. and James E. Gunn (1973). "Method for Detecting a Cosmological Density of Condensed Objects". In: *The Astrophysical Journal* 185, pp. 397–412. DOI: 10.1086/152430.

Sachs, Michael (2008). *Angles invlved in a thin lens*. URL: https://commons.wikimedia.org/wiki/File:Gravitational-lensing-angles.png#/media/File:Gravitational-lensing-angles.png (visited on 2019).

Schneider, P., J. Ehlers, and E.E. Falco (1992). *Gravitational Lenses*. Springer-Verlag. DOI: 10.1007/978-3-662-03758-4.

Sridhar, Sarrvesh S. (2013). "Modelling the Gravitationally Lensed Quasar PKS 1830-211". Chalmers University of Technology.

Subrahmanyan, R., D. Narasimha, A. Pramesh Rao, and G. Swarup (1990). "1830-211 / gravitationally lensed images of a flat-spectrum radio core ?" In: *Monthly Notices of the Royal Astronomical Society* 246, p. 263.

Umetsu, Keiichi (2010). "Cluster Weak Gravitational Lensing". In: *arXiv e-prints*, arXiv:1002.3952, arXiv:1002.3952. arXiv: 1002.3952 [astro-ph.CO].

Walsh, D., R. F. Carswell, and R. J. Weymann (1979). "0957+561 A, B: twin quasistellar objects or gravitational lens?" In: *Nature* 279, pp. 381–384. DOI: 10.1038/279381a0.

Winn, Joshua N., Christopher S. Kochanek, Brian A. McLeod, Emilio E. Falco, Christopher D. Impey, and Hans-Walter Rix (2002). "PKS 1830-211: A Face-on Spiral Galaxy Lens". In: *The Astrophysical Journal* 575.1, pp. 103–110. DOI: 10.1086/341265. arXiv: astro-ph/0201551 [astro-ph].

A

Appendix 1

A.1 Model Code

The code for GravLens module for simulating the source and the code for simulating the absorption spectra are listed in this section.

A.2 Code used for GravLens

The code for GravLens can be executed as a batch process by writing the code in a file and executing it directly with the lensmodel from the terminal directly. It can be directly executed by using the following command:
`./lensmodel <filename>`
The code for simulating PKS 1830-211 is shown next:

```
set omega   = 0.3
set lambda = 0.7
set hval    = 0.7
#
set zlens   = 0.889
set zsrc    = 2.507
set omitcore = 1
#
# alpha is SIE model, mass x y ellip PA, p[8] is the softening and
#p[10] the alpha, last param is z_lens
gridmode 1

  set rscale = 1
  set ngrid1 = 100
  set ngrid2 = 1000

  set maxlev = 2

startup 1 1
    alpha 1 0.0 0.0 0.091 87.1 0 0 0.1 0 1.0
    # Mscale, x, y ell pa 0 0 rscale 0.0 powerlaw
    0 0 0 0 0 0 0 0 0 0
```

```
setsource 2 100

     sersic 8 -0.064 0.046 0 0 0.05 0 1/4
     sersic 3 -0.063998 0.046 0 0 0.01 0 1/4
     0 0 0 0 0 0 0 0
     0 0 0 0 0 0 0 0
plotcrit clensmode1.crit
plotgrid gridfile_ISM.grid

SBmap2 -1 1 4000 -1 1 4000 1 sourcepos_molec_2.fits 3
# xlo xhi nsteps ylo yhi nsteps nover filename ftype
```

A.3 Code for simulating the absorption spectra

The code for this section was written in matlab and all the functions required are either defined or found in the matlab documentation.

```
function spectrum

%pos1
lumin1 = fitsread('sourcepos_4000.fits');
     norm_lumin1 = (lumin1);
     r1 = funr(lumin1);
     V_los1 = funvel(r1);
%pos2
lumin2 = fitsread('sourcepos_4000_2.fits');
     norm_lumin2 = flip(lumin2);
     r2 = funr(lumin2);
     V_los2 = funvel(r2);

[L B] = size(norm_lumin1);
V=linspace(-200,200,50);
I1=funI(norm_lumin1,V_los1,V);
I2=funI(norm_lumin2,V_los2,V);

Iplot(I1,I2,V);
end

function Iplot(I1,I2,V)
I_tot1=sum(I1,[1 2]);
I_1d1=I_tot1(:);
I_1d_norm1= I_1d1/max(I_1d1);

I_tot2=sum(I2,[1 2]);
I_1d2=I_tot2(:);
```

```
I_1d_norm2= I_1d2/max(I_1d2);

diff=I_1d_norm1-I_1d_norm2;

compPlot = figure('Name', 'Modelled Absorption Spectrum');
ax1 = axes('Parent', compPlot);
plot(V,I_1d_norm1, 'Color', 'blue');
hold on
plot(V,I_1d_norm2, 'Color', 'red');
hold off
%title(ax1, 'abs spectra jet pos change by 2pas');
xlabel('Velocity (Km/s)');ylabel('Intensity(normalised)');
%legend('Initial position','Change by 2pas');
figure(2);
plot(V,diff, 'Color', 'green');title('difference in absorption');
xlabel('Velocity (Km/s)');ylabel('Intensity');
end
function res = funr(lumin)

    [L B] = size(lumin);
    a=2;
    xx = linspace(-a,a,L);
    yy = linspace(-a,a,B);
    [X,Y] = meshgrid(xx,yy);
    res = sqrt((X).^2 + (Y).^2);
end

function res = funvel(r)
[L B] = size(r);
    v0 = 266; % km/s
    v1=ones(L,B);
    Vel=v0*v1;
    % inclination information
inc = 30;

    a=1;N=L;
    xx = linspace(-a,a,N);
    yy = linspace(-a,a,N);
    r2d = 180/pi;

    theta = r2d.*atan2(xx,yy);
    V_los=Vel.*cosd(theta-90).*sind(inc);
    res = V_los;
end
function res = tau(norm_lumin)
[L B] = size(norm_lumin);
```

```
%t=ones(L,B)*0.057;
t=zeros(L,B);

%generating checkerboard
%NE
imgSiz_ne = [1560,1460];
blkSiz_ne = [2,2];
numRep_ne = imgSiz_ne./blkSiz_ne;
basMat_ne = toeplitz(mod(0:numRep_ne(1)-1,2),mod(0:numRep_ne(2)-1,2));
NE_block = repelem(basMat_ne,2,2);
NE_box=rot90((NE_block),1);

%SW
imgSiz_sw = [500,1050];
blkSiz_sw = [2,2];
numRep_sw = imgSiz_sw./blkSiz_sw;
basMat_sw = toeplitz(mod(0:numRep_sw(1)-1,2),mod(0:numRep_sw(2)-1,2));
SW_block = repelem(basMat_sw,2,2);
SW_box=rot90((SW_block),1);
%imshow(SW_block);

t(2490:3949,110:1669,:)=NE_box;
t(880:1929,3150:3649,:)=SW_box;

res =flipud(t)*0.1;
end

function res = funI(norm_lumin,V_los,V)

[L B]=size(V_los);lx=length(V);
sigma = 30.0;tau0 = tau(norm_lumin);%0.076;

% z=norm_lumin>1;
% I= norm_lumin* exp(-tau0.*exp((-(V-V_los).^2)./(2*sigma^2)));
for k=1:lx
I(:,:,k) = norm_lumin.* exp(-tau0.*exp((-(V(k)-V_los).^2)./(2*sigma^2)));
end

res = I;
end
```